ELSEVIER

Contents lists available at ScienceDirect

# Construction and Building Materials

journal homepage: www.elsevier.com/locate/conbuildmat





# Evaluating GFRP bars under axial compression and quantifying load-damage correlation

Mohammadamin Mirdarsoltany, Hossein Roghani<sup>\*</sup>, Mohammad Sadegh Tale Masoule, Nima Khodadadi, Ali Ghahremaninezhad, Antonio Nanni

Department of Civil and Architectural Engineering, University of Miami, Coral Gables, FL 33146, USA

#### ARTICLE INFO

# Keywords: Compressive elastic modulus Compressive strength Compression test Fiber-reinforced polymer GFRP rebar Micro-CT Test method

#### ABSTRACT

Fiber-Reinforced Polymer (FRP) bars have become widespread in the concrete construction industry because of their superior mechanical, physical, and durability properties. Although the tensile performance of FRP bars has been well studied, only a limited number of research projects have evaluated the compressive behavior of FRP bars due, among other reasons, to the need for a standard test method. This research aims to develop a test method to apply compression at the center of the FRP bar to avoid load eccentricity effects using a steel centering fixture with a plastic 3D-printed plug. To evaluate the ultimate compressive strength and elastic modulus, two different Glass FRP (GFRP) bars, with a 12.7 mm nominal diameter, but with two different length-to-diameter ratios of 2 and 4, were considered. The effect of 3D-printed plugs and cutting surface quality was also evaluated. The main contribution of this research is providing a straightforward test set-up for obtaining the compressive behavior of GFRP bars. The results showed that the compressive strength and elastic modulus of the tested GFRP bars are considerable in a way that the elastic modulus of the G1 bars in compression was equal to the tensile elastic modulus, so neglecting the effects of these bars in designing compressive members is too conservative.

## 1. Introduction

Fiber-Reinforced Polymer (FRP) bars have become widely used in the concrete construction sector due to their non-corrosive behavior, high durability performance, stiffness-to-weight ratio, tensile strength, and lower handling and transportation costs compared to steel reinforcement. Moreover, their electromagnetic transparency makes them an excellent choice for Magnetic Resonance Imaging (MRI) rooms [1–4]. While the tensile performance of FRP bars has been investigated comprehensively, only a limited number of research projects have evaluated their behavior under compression [5-7] due to the lack of a standard test method. In recent years, some attempts have been made to develop a test method to determine the compressive behavior of the FRP bars. Alnajmi et al. [8] investigated the compressive strength of GFRP and BFRP bars. Results indicated that for both bar types, the compressive strength is significantly lower than their tensile strength and is dependent on the diameter of the bar, and a more considerable diameter results in higher compressive strength. Abed et al. [9] conducted experiments on the response of GFRP and BFRP bars under quasi-static and dynamic loads. The research aimed to provide experimental data on the dynamic behavior of the FRP bars to use in simulations of the actual behavior of reinforced concrete (RC) elements under blast and impact loads. The finding supported Alnajmi et al.'s [8] results that the compressive strength of FRP bars was lower than the corresponding tensile strength. Plevkov et al. [10] evaluated the compressive behavior of GFRP, and Carbon FRP (CFRP) bars with 10 mm diameter. The findings illustrated that the compressive modulus of elasticity of GFRP and CFRP bars was 67 % and 73 % of their tensile modulus of elasticity, respectively. Khan et al. [11] used the ASTM D695 [12] to assess the compressive and tensile behavior of CFRP and GFRP bars. Results indicated that the compressive elastic modulus of CFRP bars was 17 % larger than that of GFRP bars. Moreover, the elastic modulus of GFRP and CFRP bars in tension was 67 % and 59 % larger than their elastic modulus in compression, respectively. As for ultimate strength, the tensile strength of both GFRP and CFRP bars was 65 % and 94 % greater than their compressive strengths, respectively. The proposed test setup needs to include information regarding the load centering on the FRP samples. Deitz et al. [13] investigated the compressive behavior of GFRP

E-mail address: h.roghani@miami.edu (H. Roghani).

 $<sup>^{\</sup>ast}$  Corresponding author.

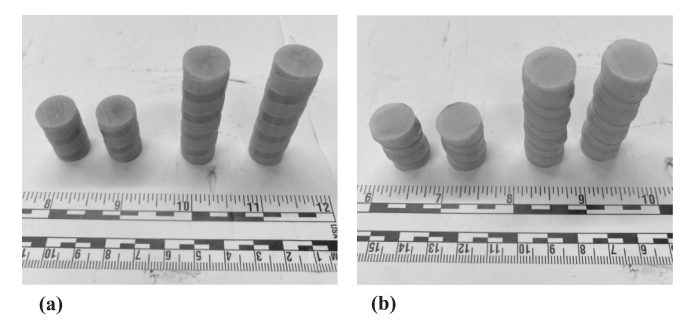


Fig. 1. Tested GFRP bars: (a) G1 coupons; and (b) G2 coupons.

bars. This research observed three distinct failure mechanisms for GFRP bars under compression: crushing, buckling, or a combination of both. In addition, outcomes revealed that 50 % of the failure modes were caused by crushing. The authors reported a similar modulus of elasticity in tension and compression. Another study was conducted by Khorramian and Sadeghian [14] and a test method was also developed. The results illustrated that the compressive modulus of GFRP is approximately the same as the tensile modulus. The compressive behavior of GFRP bars was examined by AlAjarmeh et al. [15] at elevated in-service temperatures, ranging from 23  $^{\circ}$ C to 140  $^{\circ}$ C, which could soften the polymer matrix and change the mechanical properties of GFRP bars. Results indicated that the failure mode could shift from fiber to matrix failure as the temperature rose.

According to the current literature, there are divergencies between the results of the compressive behavior of FRP bars, ranging from compressive strength and compressive modulus of elasticity to ultimate compressive strain and stress-strain curve, and this is mainly due to the need for a standard test. Due to inconclusiveness in the available literature, the contribution of FRP bars to the capacity of concrete columns reinforced with FRP is neglected, and ACI 440.11-22 [16] states that "The area of GFRP reinforcement in compression shall be treated as having the same strength and stiffness as the concrete in the surrounding compression zone." The AASHTO LRFD Bridge Design Guide Specifications for GFRP-Reinforced Concrete [17] has a more conservative statement that ignores the compressive strength of GFRP reinforcements in design calculations [14]. The test setups in the literature show that preparing samples for compression testing is complicated. For instance, in the research conducted by AlAjarmeh et al. [18] and another research by Khorramian and Sadeghian, steel tubes are used at both ends of the coupon and it is required to fill them with grout or adhesives before FRP samples are inserted. These methods require significant preparation time and the disposal of the steel tubes. Another notable neglection in some test methods is the absence of means for applying load to the center of the sample. Moreover, when the sample is inserted directly into the steel tube, the confinement resulting from the stiffness of the steel tube affects the compressive behavior.

This research project aims to provide a simple test setup to determine FRP bars' compressive strength and elastic modulus, ensuring that the



(a)



Fig. 2. Samples before ignition: (a) G1; and (b) G2.

load is applied at the center of the coupon. 3D-printed plugs made of Polylactic Acid (PLA) and Thermoplastic Polyurethane (TPU) filament are used to fill the gap between the FRP samples and the centering steel fixture, thus minimizing confinement effects. As the material used to print the plugs is much softer than steel materials and it minimizes the confinement. This research investigates two GFRP bar types, coupon length-to-diameter ratios of 2 and 4, two 3D-printed plug materials, two inner diameters of the plugs, and cutting surface quality. Choosing the length-to-diameter ratios of 2 and 4 ensures that the failure mode is GFRP coupon crushing rather than the buckling of the coupon or the microbuckling of individual fiber buckling. This results in determining the pure compressive strength of the material and helps achieve the ultimate capacity of the bar in compression.

# 2. Experimental program

#### 2.1. FRP rebars

In this study, two different types of GFRP, named G1 and G2, all having a nominal diameter of 12.7 mm (0.5 in.), were selected to be evaluated under uniaxial compression. G1 bars are grooved (fibers are

**Table 1**Evaluated properties, test methods, and the acceptance criteria for the tested FRP rebars.

	-		
	Property	Test Method	Acceptance Criteria*
Physical properties	Measured cross-sectional area	ASTM D792	$\begin{array}{l} 119 \ \text{mm}^2 \ [0.185 \ \text{in.}^2] \leq A_b \\ \leq 169 \ \text{mm}^2 \ [0.263 \ \text{in.}^2] \end{array}$
	Fiber content	ASTM D2584	≥ 70 %
	Ultimate tensile strength		744.2 MPa [108ksi]
Mechanical properties	Ultimate tensile strain	ASTM D7205	$\geq 1.1$ %
	Tensile elastic modulus		≥ 44.8 GPa [6.5 Msi]
*Based on ASTM D7957 and FDOT 932-3			

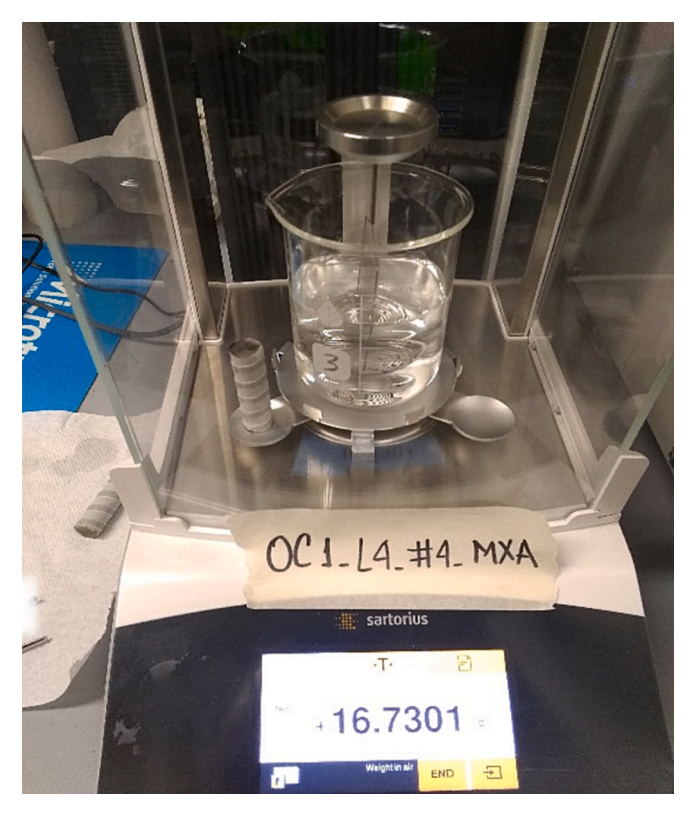


Fig. 3. ASTM D792 test setup.

not continuous) to make the surface enhancement, and in G2 bars, the surface enhancement is provided by integral ribs (fibers are continuous). In addition to considering bars from different manufacturers, two different length-to-diameter ratios were assessed (see Fig. 1). The bars'



Fig. 4. Tensile test setup according to ASTM D7205.

physical and mechanical characteristics were considered per the test methods listed in ASTM D7957 [19] and FDOT 932–3 [20]. The evaluated properties, test methods, and acceptance criteria are represented in Table 1.

Although the focus of this paper is the characterization of GFRP bars in compression, the results of other characterization tests such as cross-sectional area, fiber content, and tensile behavior, pertinent to the minimum requirements of ASTM D7957 specifications, are required for the compression test results to be validated.

#### 2.2. Fiber mass content

ASTM D2584 [20] was employed to determine the fiber mass content. For each type of FRP bar, three samples were cut to 25.0 mm (1.0 in.) (see Fig. 2). ASTM D2584 requires the burn-off procedure in which the FRP bars are exposed to  $565 \pm 28\,^{\circ}\text{C}$  ( $1050 \pm 50\,^{\circ}\text{F}$ ) temperature so that the resin matrix burns off, leaving the fibers, fillers, and materials used to provide surface enhancements in the crucible. The fiber mass content is then determined by dividing the weight of the residual after ignition by the initial weight of the specimen.

#### 2.3. Measured cross-sectional area

The ASTM D792 [21] was used to determine the cross-sectional area of the bars. The cross-sectional area of M13 (No. 4) bars must be within the range of  $119\,\mathrm{mm}^2$  [0.185 in.²] and  $169\,\mathrm{mm}^2$  [0.263 in.²] as per ASTM D7957 [21] and FDOT 932–3 [20]. The density of test samples is measured using the water displacement principle. The specimen's mass in air and water is required to determine the specific gravity and density. The volume of the specimen is calculated by dividing the mass by the measured density. To calculate the cross-sectional area, the obtained volume should be divided by the length of the sample. Fig. 3 shows the test setup for measuring the cross-sectional area.

The tensile properties of FRP bars were evaluated in accordance with the provisions of ASTM D7205 [22]. For each type of bar, three specimens were cut to a length of 1270 mm (50.0 in.). ASTM D7205 requires rigid pipe-shaped anchors at both ends of the bar as an interface layer between the grip and the FRP bar; therefore, steel pipes having an outer diameter of 42 mm (1.63 in.), a thickness of 5.08 mm (0.2 in.), and a length of 375 mm (15 in.) are used and filled with expansive grout. A vertical Universal Testing Machine (UTM) with a maximum capacity of 2000 kN (450 kips) was used to test the bars (see Fig. 4), and a 100 mm (4.0 in.) extensometer installed in the middle of the bar to measure the tensile strain.

# 2.4. Compressive test

A total number of 50 specimens with different length-to-diameter ratios, plug materials, and cutting surface quality were prepared. Moreover, four additional samples of type G1 were used to investigate the crack patterns, failure modes, and correlation between applied load and damage. In terms of plug materials, specimens with a length-todiameter ratio of 2 were divided into three groups: the first group tested with tight 3D-printed plugs with Polylactic Acid (PLA) filament; the second group tested with loose PLA 3D-printed plugs, and the third group tested with tight 3D-printed plugs with Thermoplastic Polyurethane (TPU) filament. The tight plugs with an inner diameter closer to the measured diameter of each bar type provide more confinement. The plug inner diameter for each bar type and the filament types utilized to print the plugs are presented in Table 2. Tight PLA plugs were used for the coupons with a length-to-diameter ratio of 4. Two different cutting approaches were used, namely a diamond-blade wet saw and a chop saw. In the former approach, the bars were firmly clamped to a guide during cutting to ensure parallelism of the top and bottom faces within  $\sim$ 50  $\mu m$  as measured using a digital caliper with an accuracy of 10  $\mu m$ (Mitutoyo, Inc.). As for the latter approach, the bars were placed on the

**Table 2** 3D-printed plugs properties.

Filament type	Filament Diameter mm [in.]	Print Infill %	Tensile Strength Mpa [psi]	Group	Bar Type	Inner diameter of plug mm [in.]
			62 [8990]	Tight	G1	0.56 [0.022]
PLA	1.75 [0.069]	10		Hight	G2	0.60 [0.024]
PLA	1.75 [0.069]	10		Loose	G1	0.58 [0.023]
					G2	0.63 [0.025]
	0.00.50.1141	5	23.7 [3440]	Tight	G1	0.56 [0.022]
TDLI					G2	0.60 [0.024]
TPU	2.90 [0.114]			Loose	G1	0.58 [0.023]
					G2	0.63 [0.025]
-						

chop saw. There was no precise approach to ensuring the bottom and top surfaces were parallel. It should be noted that cutting quality is important to avoid premature failure, undesirable moments, and inconsistent results. The test setup and testing fixtures are illustrated in Fig. 5.

The outer and inner diameters of the steel centering fixture were 50.8 mm (2 in.) and 25.4 mm (1 in.), respectively, with a central cavity depth of 12.7 mm (0.5 in.), which is dependent on the nominal diameter of the bar. Similarly, the inner diameter and height (12.7 mm) of the 3D-printed plug depend on the surface enhancement and the measured coupon's diameter. In contrast, the plug's outer diameter corresponds to the centering fixture's inner diameter. The centering fixture is directly installed on the movable crosshead of the UTM. The function of the plastic plug is to fill the gap between the coupon and the centering fixture, limiting the confinement effect provided by steel. To avoid premature failure, undesirable moments, and inconsistent results, both ends of the FRP coupon were machined flat and perpendicular to the

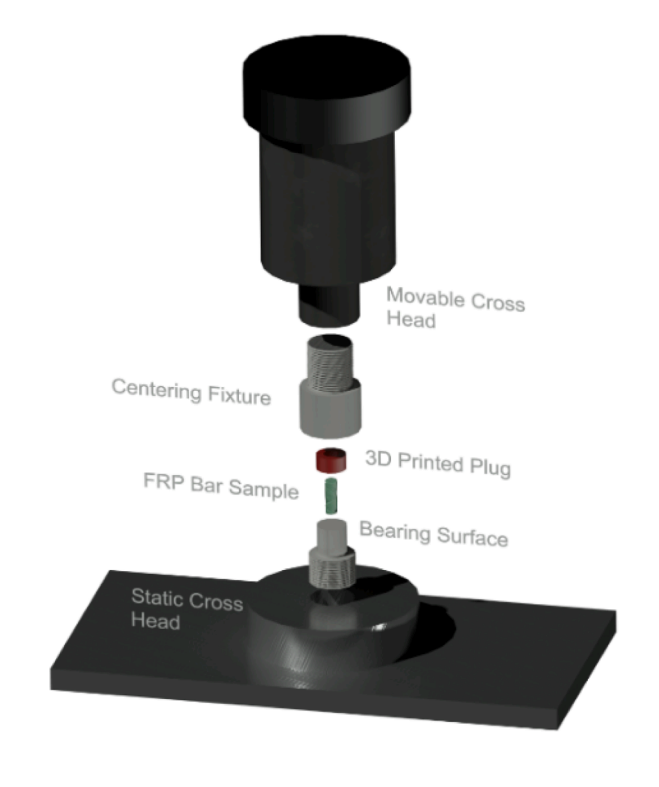
longitudinal axis. However, during the cutting procedure, the quality of the cut surfaces by the chop saw (CS) was less than that of the diamond-blade wet saw (DWS).

After obtaining the compressive strength of GFRP bars by the proposed test method, six more G1 coupons were prepared to obtain their elastic modulus in compression and compare the result with the tensile elastic modulus. Fig. 6 shows the test setup for getting the compressive elastic modulus of G1 bars using a laser extensometer.

#### 2.5. Micro-computed tomography

After determining the ultimate compressive strength of type G1 bars, three additional coupons with a length-to-diameter ratio of four were subjected to 25, 50, and 75% of the ultimate compressive load to quantify the damage and investigate the applied load-damage correlation. A micro-computed tomography (Micro-CT) analysis was performed





**(b)** 

Fig. 5. Compressive strength test setup: (a) actual test setup; and (b) schematic overview of test setup.

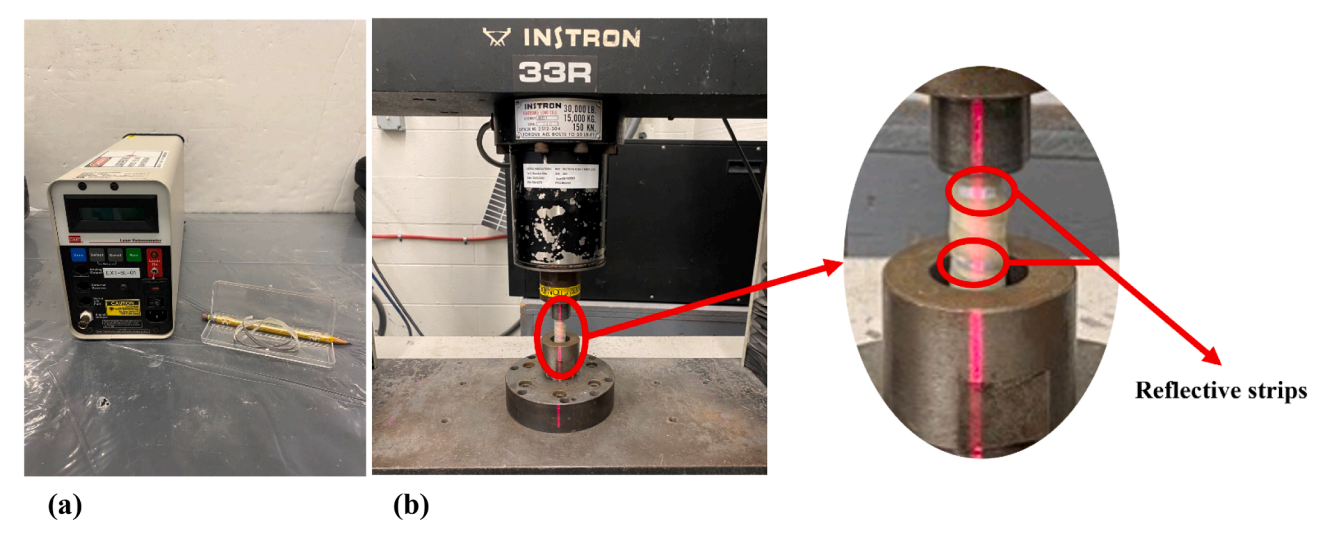


Fig. 6. Laser extensometer for strain measurements: (a) device and reflective strips; and (b) setup.

**Table 3** Physical and geometrical properties of GFRP rebars.

Bar Type	Bar Designation No.	Fiber Type	Nominal Diameter mm [in.]	Nominal Cross-Sectional Area mm <sup>2</sup> [in. <sup>2</sup> ]	Measured Cross-Sectional Area		Fiber Mass Content %	
					Ave. mm <sup>2</sup> [in. <sup>2</sup> ]	CoV (%)	Avg %	CoV (%)
G1 G2	M13 [4] M13 [4]	Glass Glass	12.7 [0.50]	129 [0.20]	148.5 [0.230] 168.4 [0.261]	0.5 0.8	83.2 78.9	0.2 0.4

**Table 4**Tensile properties of GFRP rebars.

Bar	Ultimate Tensile		Mean U	Iltimate	Tensile Elastic Modulus	
Type	Strength		Tensile	Strain		
	Ave. MPa	CoV	Ave.	CoV	Ave. GPa	CoV
	[ksi]	(%)	%	(%)	[Msi]	(%)
G1	1038.9 [150.7]	0.9	1.77	3.8	58.7 [8.51]	4.4
G2	1132.9 [164.3]	4.9	1.73	5.7	65.7 [9.53]	1.1

on these three samples using a Bruker SkyScan 1273. The projections were collected at a pixel size of  $15\,\mu m$  with a 0.3 mm-thick filter at a voltage and amperage of 110 kV and 136 $\mu A$ , respectively. The exposure time was 1100 ms, and ten frames were averaged at each 0.5° angle. The final segmentation and analysis of the 3D microstructure were done using a grayscale range of 0–130 for imperfections and cracks in the Bruker CTAn software.

# 3. Test results

# 3.1. Fiber mass content test

Both FRP bar types used in this study met the minimum requirements established by ASTM D7957 and FDOT 932–3. Table 3 shows the fiber mass contents.

# 3.2. Measured cross-sectional area

The measured cross-sectional area of the two bar types (see Table 3) was compared to the acceptance criteria in Table 1. The results were within the range given by ASTM D7957 and FDOT 932–3.

# 3.3. Tensile test

For the two bar types, the ultimate tensile strength calculated by dividing the ultimate tensile load by the nominal cross-sectional area exceeded the minimum limits provided by ASTM D7957 and FDOT

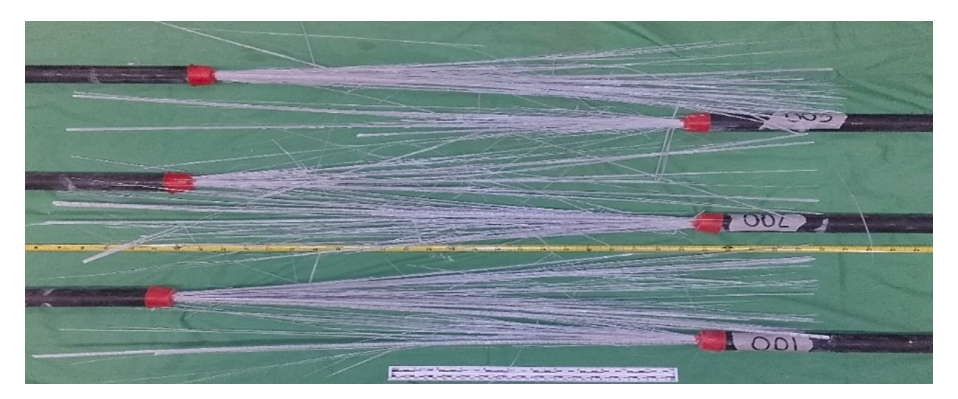


Fig. 7. Typical failure of GFRP bars after tensile test.

**Table 5**Compression test results.

Specimen ID	Type of Plug	Length-to-diameter ratio	Cutting type	Compressive strength (MPa)	Average compressive strength	Average tensile to compressive strength
G1-T-P-4-1				715.7		
G1-T-P-4-2			CS	620.5	612.8	1.7
G1-T-P-4-3			CS	587.4	612.8	1./
G1-T-P-4-4				527.4		
G1-T-P-4-5				753.2		
G1-T-P-4-6				875.5		
G1-T-P-4-7				851.6		
G1-T-P-4-8	Tight PLA	4	DWS	886.9	847.2	1.2
G1-T-P-4-9	Ü			846.4		
G1-T-P-				869.6		
4–10						
G2-T-P-4-1				432.3		
G2-T-P-4-2			00	455.1	454.4	0.4
G2-T-P-4-3			CS	495	474.4	2.4
G2-T-P-4-4				515		
G1-T-P-2–1				804.6		
G1-T-P-2–2			00	688.8	705 F	1.5
G1-T-P-2–3			CS	621.9	705.7	1.5
G1-T-P-2-4				707.4		
G1-T-P-2-5				863.2		
G1-T-P-2–6				865.3		
G1-T-P-2-7				889.5		
G1-T-P-2–8			DWS	852.7	851.4	1.2
G1-T-P-2–9				764.3		
G1-T-P-				873.5		
2-10						
G2-T-P-2-1	Tight PLA	2		457.8		
G2-T-P-2-2				543.3		
G2-T-P-2-3			CS	536.4	530	2.1
G2-T-P-2-4				582.6		
G2-T-P-2-5				723.1		
G2-T-P-2-6				784.3		
G2-T-P-2-7				787.3		
G2-T-P-2-8			DWS	654.2	730	1.6
G2-T-P-2-9				698.6		
G2-T-P-				732.3		
2-10						
G1-L-P-2–1				496.4		
G1-L-P-2–2			CC	504	532.6	2
G1-L-P-2-3			CS	525.4	532.0	2
G1-L-P-2-4	Loose DI A	2		604.7		
G2-L-P-2-1	Loose PLA	۷		448.8		
G2-L-P-2–2			CS	422.6	417.9	2.7
G2-L-P-2-3			CS	415.8	417.3	4.7
G2-L-P-2-4				382		
G1-L-P-2–1				573.6		
G1-L-P-2–2			CC	503.3	511.6	2
G1-L-P-2–3			CS	486.8	511.0	2
G1-L-P-2-4	Tieks TDII	0		482.6		
G2-L-P-2–1	Tight TPU	2		417.8		
G2-L-P-2-2			00	399.2	205.2	2.0
G2-L-P-2-3			CS	399.2	395.2	2.9
G2-L-P-2-4				364.7		

932–3. Table 4 shows the tensile properties, while Fig. 7 shows typical failure of GFRP bars in tension.

# 3.4. Compressive strength

Table 5 shows the results of compression tests. Coupons with tight PLA plugs and a length-to-diameter ratio of 4 have a compressive strength lower than coupons with tight PLA plugs and a length-to-diameter ratio of 2 due to the coupon slenderness compared to the coupons with a length-to-diameter ratio of 2. Coupons with a length-to-diameter ratio of 2 with tight PLA plugs show the highest compressive strength. Moreover, results showed that the FRP bars' compressive strength depends on the cutting surface's quality. The compressive strength of FRP bars will increase with surface flatness and parallelizing

of the top and bottom faces of the coupon.

According to the results from samples with a length-to-diameter ratio of 2, the type of filament used to 3D print the plugs and their inner diameter have an influence on the compressive strength. In fact, the average compressive strength of samples with tight PLA plugs is the highest, possibly due to higher confinement effects as tight PLA plugs are stiffer than tight TPU plugs.

In fact, the FRP samples with loose PLA plugs have more space to expand under compressive load, and the confinement effect would be lower than the tight PLA plugs. This confinement is why samples with tight PLA plugs reach higher compressive strengths than those with loose PLA plugs. Fig. 8 shows the samples after the compression test.

Regarding the type of cutting, samples with DWS-cut and parallelized ends showed higher compressive strength than their CS-cut

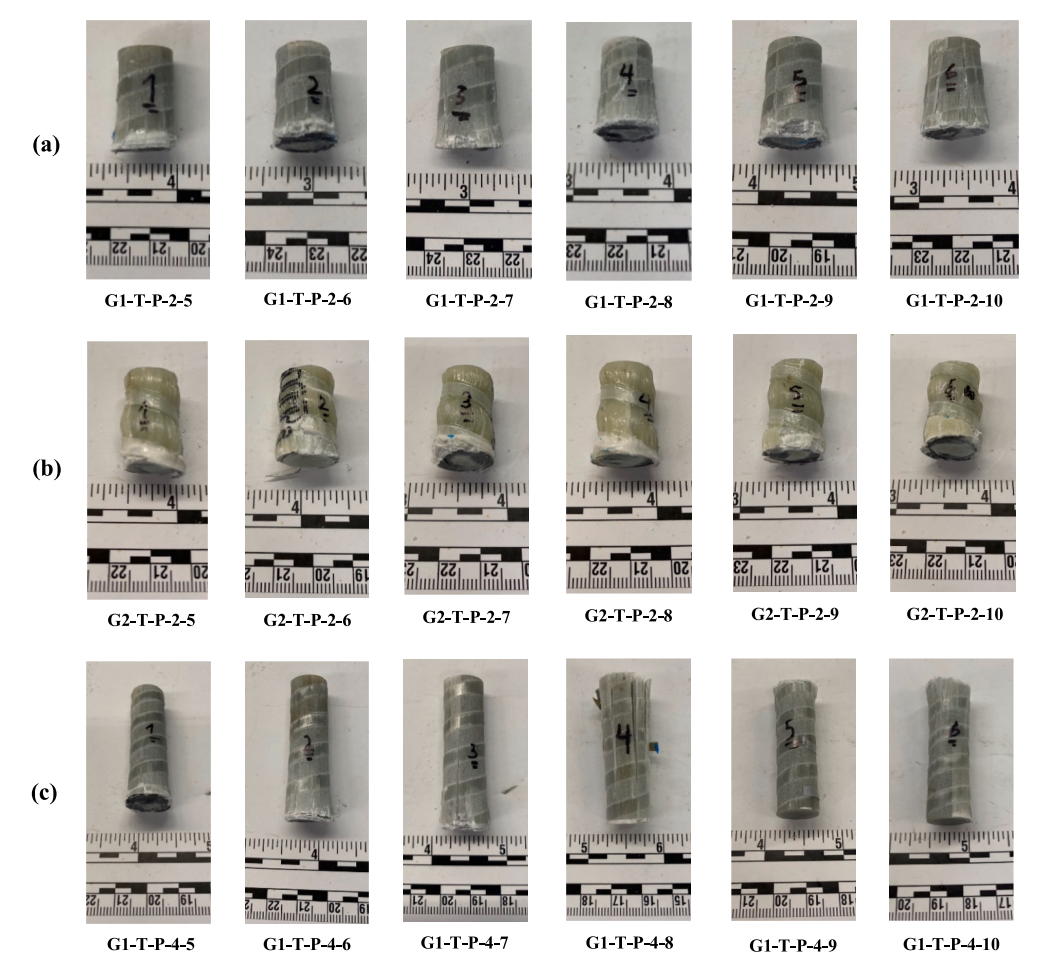


Fig. 8. Specimens after compressive test.

counterparts. It is because of uniformly applied loads on the cross-section of the coupons with high-quality surfaces. Moreover, the compressive results in coupons with DWS-cut are more consistent than those with CS-cut.

Fig. 9 shows boxplots of compressive strength data illustrating the data distribution for each group of coupons. According to this figure, one could observe that specimens prepared by diamond-blade wet saw resulted in higher compressive strength than those equipped with the chop saw. In addition, tight PLA 3D-printed plugs help the coupons reach their ultimate capacity before failure. In most specimens, the failure occurred at the end of the bar in the 3D-printed plug (see Fig. 10).

# 3.5. Compressive modulus of elasticity

Three G1 FRP bars were tested under compression to obtain the compressive elastic modulus. As shown in Fig. 11, the surface of the G2 bars was wavy and not smooth, causing issues for measuring strain. Moreover, the cross-section of this bar was not a perfect circle, so G1 bars were chosen over G2 bars to investigate the compressive elastic modulus. Fig. 12 shows the stress–strain curves of the G1 coupons under compression. The graph shows that the stress–strain curves for all the samples are consistent. Moreover, it shows that the proposed test setup applies to capture the FRP bars' compressive elastic modulus.

According to Table 6, the compressive elastic modulus of tested FRP

bars is similar to their tensile elastic modulus. Obtaining the compressive strength and elastic modulus of FRP bars under compression shows that neglecting their contribution to the compressive strength of compressive members is a conservative design approach.

# 3.6. Damage correlation and micro-computed tomography

After obtaining the ultimate compressive strength of GFRP bars, three samples of the G1-type FRP bars were loaded to 25 %, 50 %, and 75 % of their ultimate compressive strength. Micro-CT and dye penetration approaches are applied to observe crack propagation at each level of applied loads. Although the crack pattern was not detected by dye penetration, the Micro-CT could show the crack patterns and damage to the coupons. Table 7 shows the ultimate capacity of the samples and the corresponding loads at 25 %, 50 %, and 75 % of the ultimate capacity.

Studying the internal damage in the GFRP coupons under compression is important to investigate the failure modes, load-damage correlation, and crack propagation. Micro-CT is a powerful, non-destructive method of visualizing and accurately analyzing the change in the microstructure of matter, capable of characterizing objects as small as a few micrometers.

Figs. 13 and 14 display the propagation of damage in the GFRP coupons as they are subjected to increasing levels of compressive load.

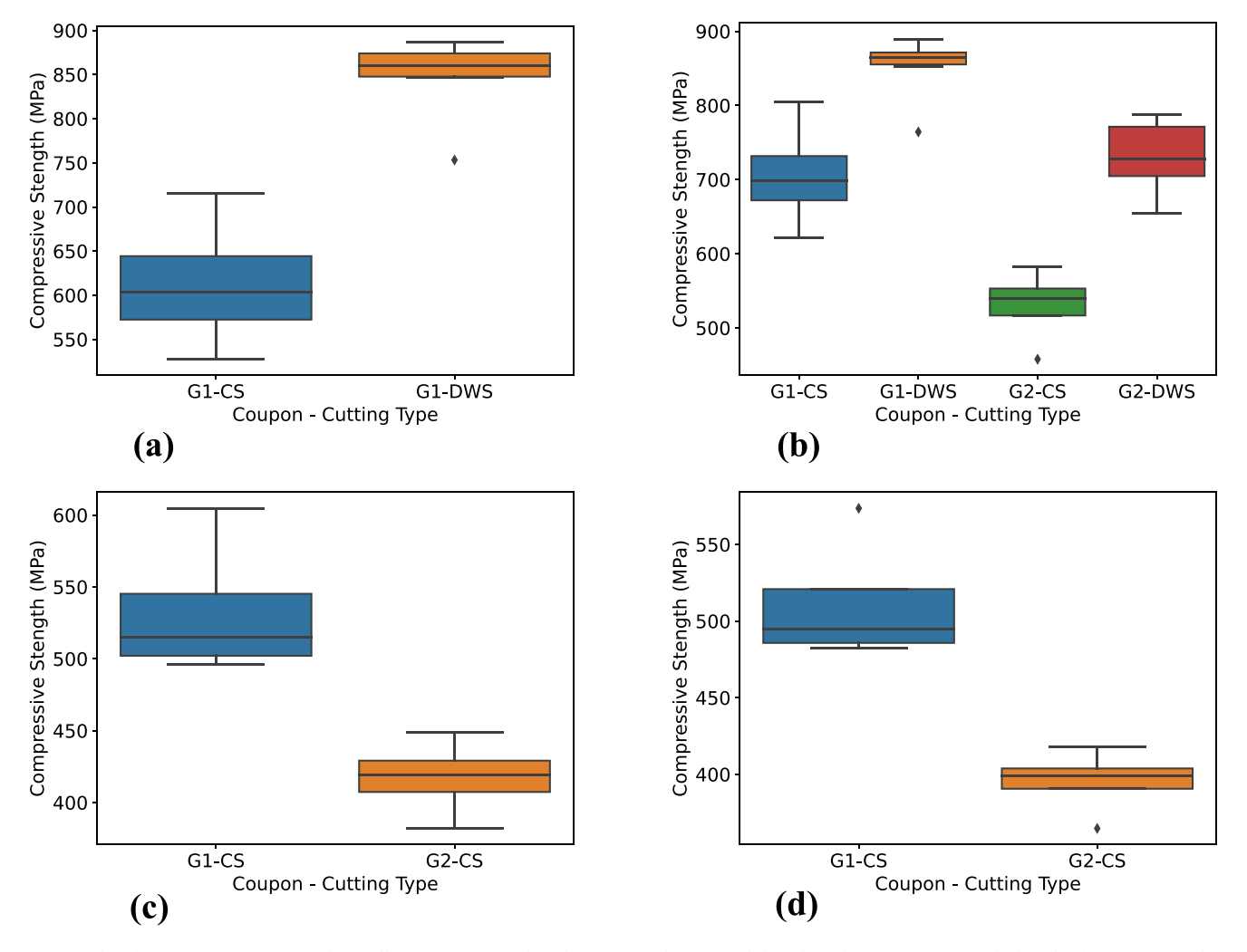


Fig. 9. Box plots for comparison of strength for all experiments: (a) boxplot for G1-tight PLA with length-to-diameter ratio = 4; (b) boxplot for G1 & G2 tight PLA with length-to-diameter ratio = 2; and (d) boxplot for G1 & G2 tight TPU with length-to-diameter ratio = 2.

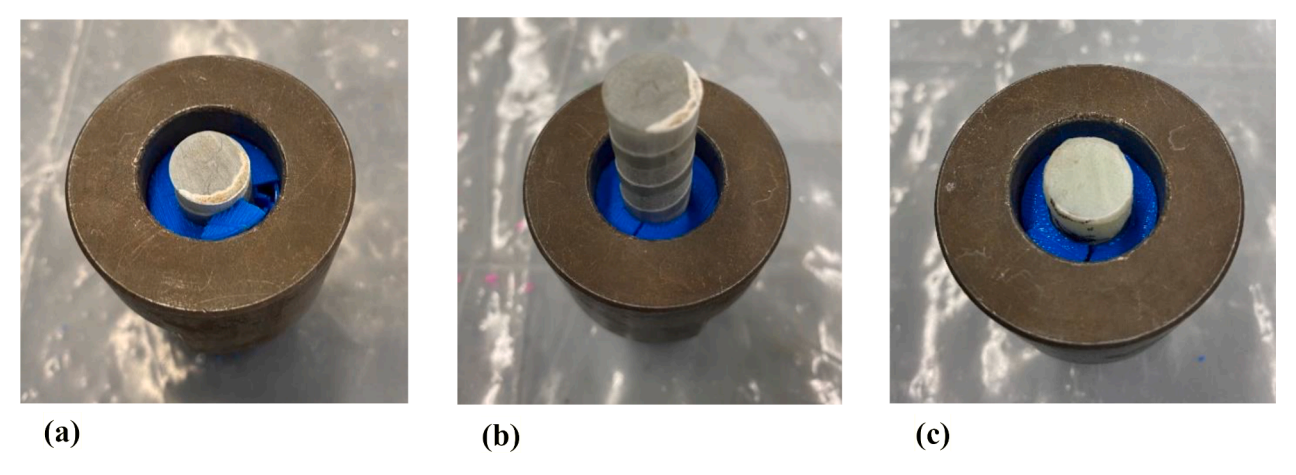


Fig. 10. Failure of the coupons at the end with 3D-printed plug: (a) G1-T-P-2-7; (b) G1-T-P-4-7; and (c) G2-T-P-2-10.



Fig. 11. Surface profile of G2 bar.

At 25 % and 50 % lower loading levels, no cracking is observed, and the voids (black regions) are only composed of imperfections and gaps in the resin matrix (white regions) produced during the manufacturing process. While manufacturing imperfections are prevalent in the lower spectrum, hairline cracks are first observed at 75 % of loading, as evident by the void geometries in Fig. 14 (b) which only show a low amount of crack volume compared to the imperfections. These hairline cracks propagate into a fully connected network of large cracks at peak load, and large quantities of interconnected cracks occupy the specimen, which is seen in Fig. 14 (b) as several multi-directional plates joined into a single object.

Fig. 15 summarizes the quantitative analysis performed on the 3D model of voids in the GFRP coupon using CTAn software with different loading levels. Fig. 15 (a) shows the increase in crack width from 0 at loads below 50 % to 0.33 mm at the peak. This value is the average width between all instances of cracks with varying sizes and includes cracks with different thicknesses from hairline to those as wide as 1 mm. Fig. 15 (b) and (c) show the change in volume fraction and surface area of the voids, respectively, where the minimum change was observed prior to the peak. A very small increase in crack volume is seen at 75 % loading, but it's insignificant compared to the peak increase, showing that most cracks develop in the 75 %–100 % range.

## 4. Statistical analysis

In statistical analysis, particularly within the domains of hypothesis testing and regression, the p-value and the t-statistic are pivotal. The following provides a succinct elucidation of their derivation [23,24]. The t-statistic is employed when conducting a t-test, a statistical method that assesses whether the average values of two groups differ significantly. For a two-sample t-test, the equation to compute the t-statistic is:

$$t = \frac{\bar{X}_1 - \bar{X}_2}{\sqrt{\frac{s_1^2}{n_1} + \frac{s_2^2}{n_2}}}$$

where  $\bar{X}_1$  and  $\bar{X}_2$  represent the means of the two samples,  $s_1^2$  and  $s_2^2$  stand for the variances of these samples, and  $n_1$  and  $n_2$  indicate the number of observations in each group. The *p*-value serves as an indicator of the significance of results in hypothesis testing, representing the strength of

**Table 6**Elastic modulus of G1 bar.

ID	Tensile elastic modulus (E <sub>t</sub> ) MPa	Compressive elastic modulus (E <sub>c</sub> ) Mpa	Average (E <sub>c</sub> ) MPa
G1-T-P-4-8 G1-T-P-4-9	58.7	57.1 57.0	58.7
G1-T-P-4-10		62.1	

**Table 7**Different load levels applied on G1 samples.

Specimen ID	Applied Load kN [kip]	Ultimate compressive load kN [kip]
G1-25	22.2 [5]	88.9 [20]
G1-50	44.4 [10]	88.9 [20]
G1-75	66.7 [15]	88.9 [20]

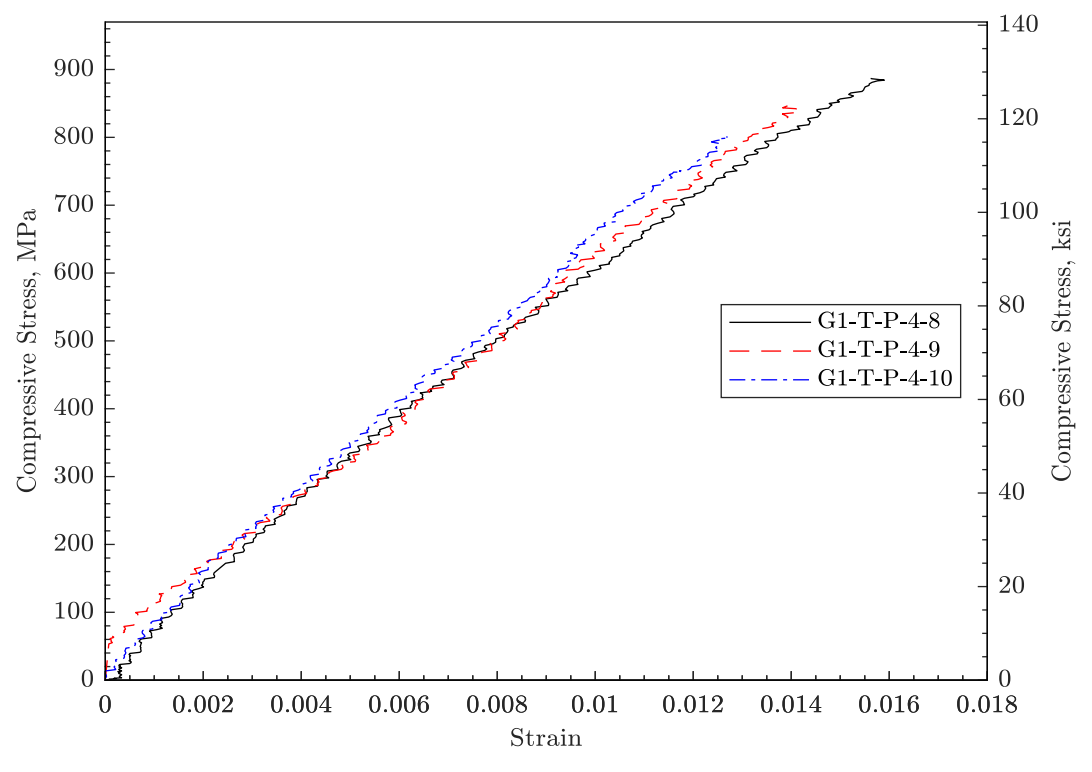


Fig. 12. Stress-strain curves of G1 coupons.

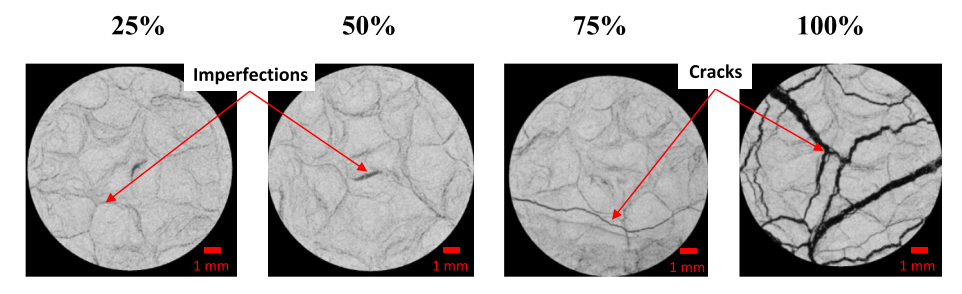


Fig. 13. Cross-sectional view of FRP bars at various loading ratios (25% to 100% of the peak load).

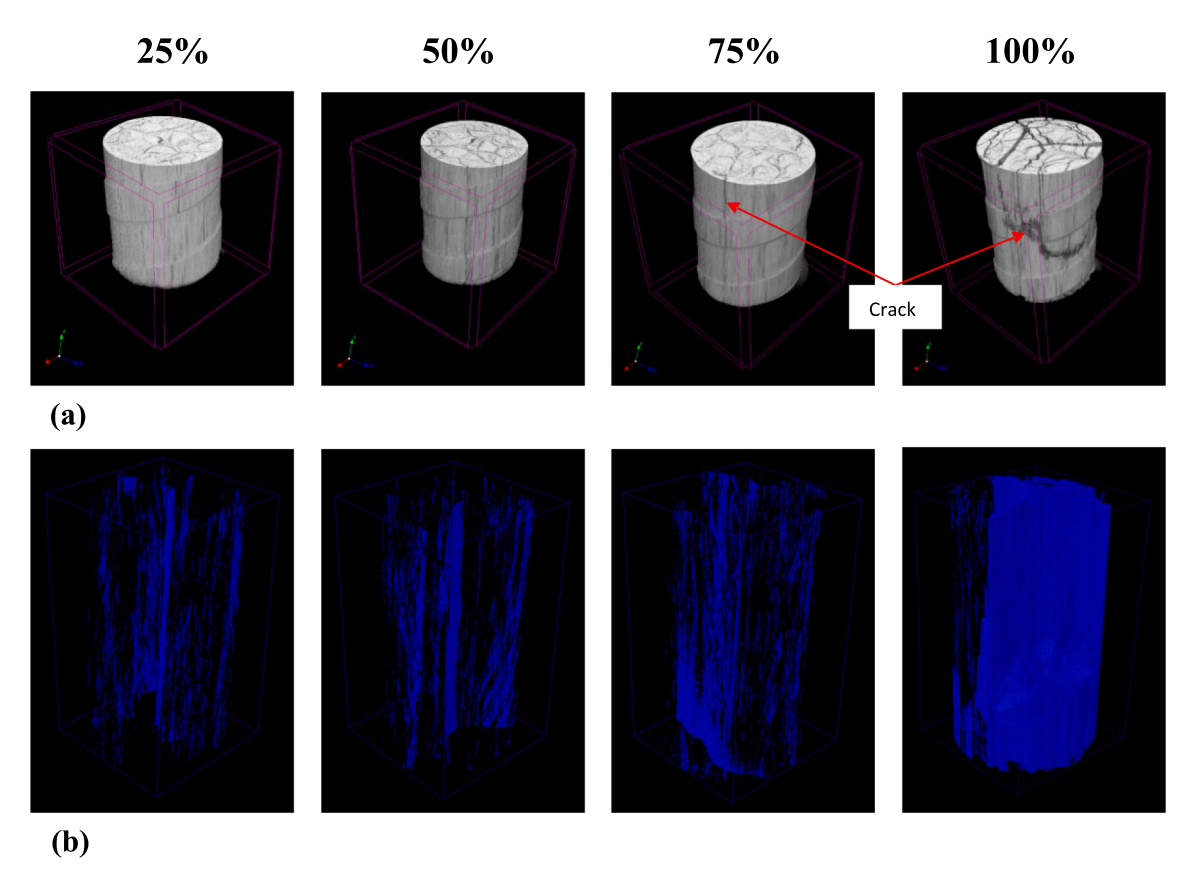


Fig. 14. 3D rendering of (a) GFRP coupon; and (b) void morphology of cracks and imperfections.

evidence against the null hypothesis. A smaller p-value suggests more compelling evidence to reject the null hypothesis. To derive it, one first computes the test statistic, such as the t-statistic. This statistic is then contrasted with a specific distribution, like the t-distribution, to gauge the likelihood of encountering a test statistic as or more extreme than the observed value, given that the null hypothesis is accurate.

The *P*-value is a fundamental concept in statistical hypothesis testing, serving as a measure to help determine the evidence against a null hypothesis. In essence, the *P*-value quantifies the probability of obtaining an observed result, or more extreme, when the null hypothesis is true. A smaller *P*-value indicates more substantial evidence against the null hypothesis, suggesting that the observed result is unlikely to have occurred by random chance alone. Typically, a threshold (often set at 0.05) is chosen below which the *P*-value is considered statistically significant, leading researchers to reject the null hypothesis in favor of an alternative hypothesis. One can employ statistical tests for an in-depth

evaluation to identify significant disparities between the outcomes of explements. This paper employs the Paired T-test for such a statistical comparison, with the resulting P-values presented in Table 8. If a value exceeds 0.05, it suggests that the two compared experiments do not show significant differences as per this test. Conversely, a P-value below 0.05 indicates a marked statistical variance between the performances of the two experiments. Based on Table 8, all P-values are less than 0.05.

Fig. 16 illustrates a circular bar plot evaluating all experiments that have a length-to-diameter ratio of 2; the cutting type designated as DWS consistently outperforms others. Furthermore, the tight PLA stands out, achieving the highest compressive strength among all other plug types. Notably, based on this chart, the G1-tight PLA DWS holds the top position. In summary, the combination of using the DWS cutting method alongside the Tight PLA plug type consistently yields the best performance in all tests.

A comparison between the two groups, G1-Chop Saw and G2-Chop

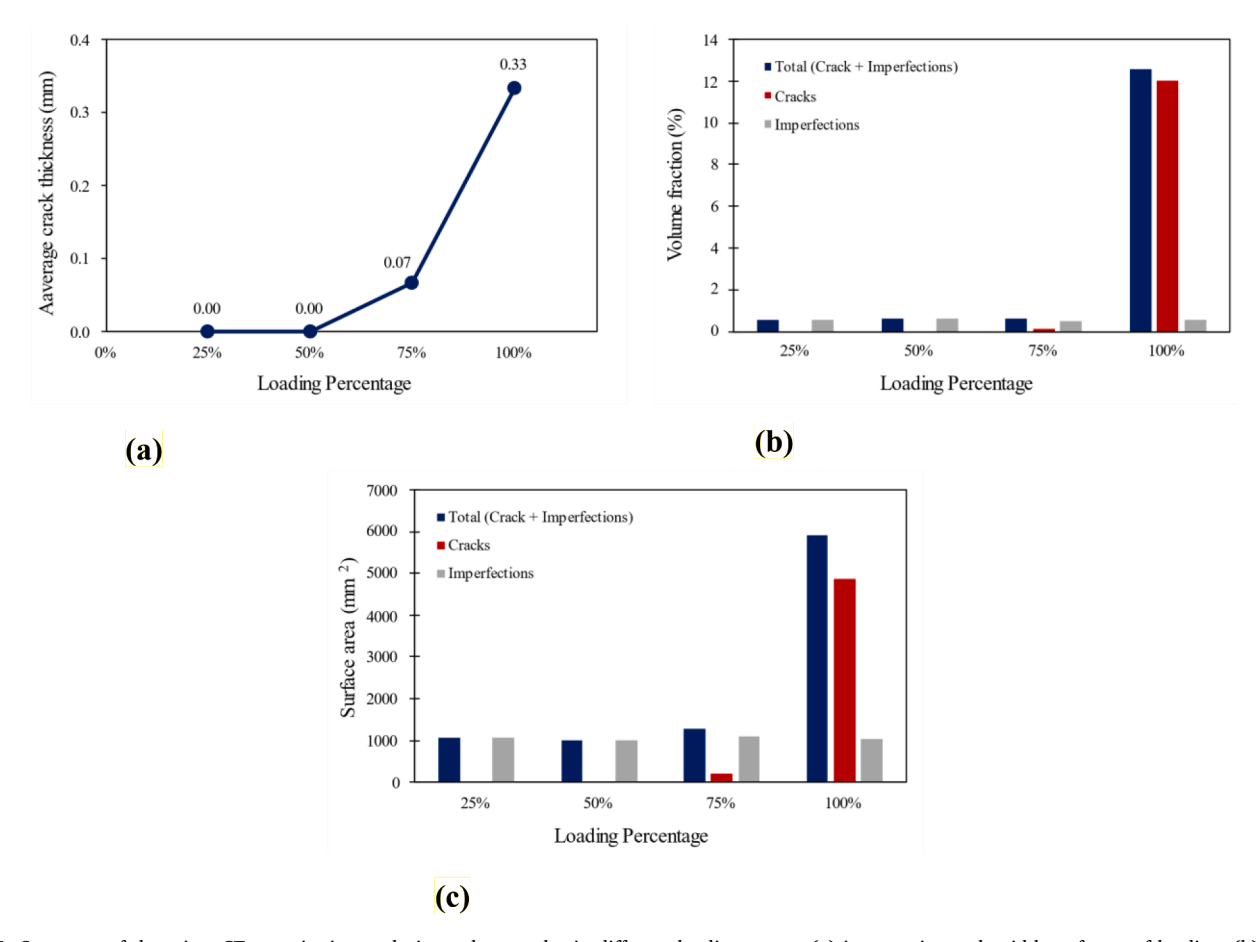


Fig. 15. Summary of the micro-CT quantitative analysis on the samples in different loading stages: (a) increase in crack width as factor of loading; (b) volume fraction of voids; and (c) surface area of the voids of the specimen.

**Table 8**The *P*-Value obtained by *T*-test for all experiments.

Tests	Cutting type	Type of plug	Length-to-diameter ratio	T-statistic	P-Value
G1 vs. G2	CS	Tight PLA	4	3.1748	0.0192
G1	CS vs. DWS	Tight PLA	4	5.8997	0.0003
G1 vs. G2	CS	Tight PLA	2	3.8262	0.0086
G1 vs. G2	DWS	Tight PLA	2	4.3980	0.0013
G1	CS vs. DWS	Tight PLA	2	3.8898	0.0046
G2	CS vs. DWS	Tight PLA	2	6.0151	0.00029
G1 vs. G2	CS	Loose PLA	2	4.0673	0.0065
G1 vs. G2	CS	Tight PLA	2	4.8726	0.0027

Saw, both have a length-to-diameter ratio of 2, as presented in the radar chart in Fig. 17. It is clear that G1 has a distinct advantage over G2 in terms of performance. Moreover, while both G1 and G2 demonstrate impressive outcomes with the tight PLA, G1 consistently outperforms G2.

# 5. Conclusion

The lack of a proper test method to determine the compressive behavior of FRP bars is one of the reasons preventing their consideration in the design of compressive members. The overarching goal of this paper is to provide a test setup to measure the compressive strength and compressive elastic modulus of GFRP bars in order to eventually pave the way for the inclusion of these characteristics in ASTM D7957. This paper studied two types of GFRP bars, both having the same nominal diameter of 12.7 mm (0.5 in.), under compression. In addition, two different length-to-diameter ratios of 4 and 2 were considered with different cutting approaches. The results showed that the GFRP bars' compressive strength depends on the length-to-diameter ratio, plug material, and cutting approaches. Increasing length-to-diameter ratio reduces the ultimate compressive strength of GFRP bars due to the increasing probability of buckling of fibers under compression.

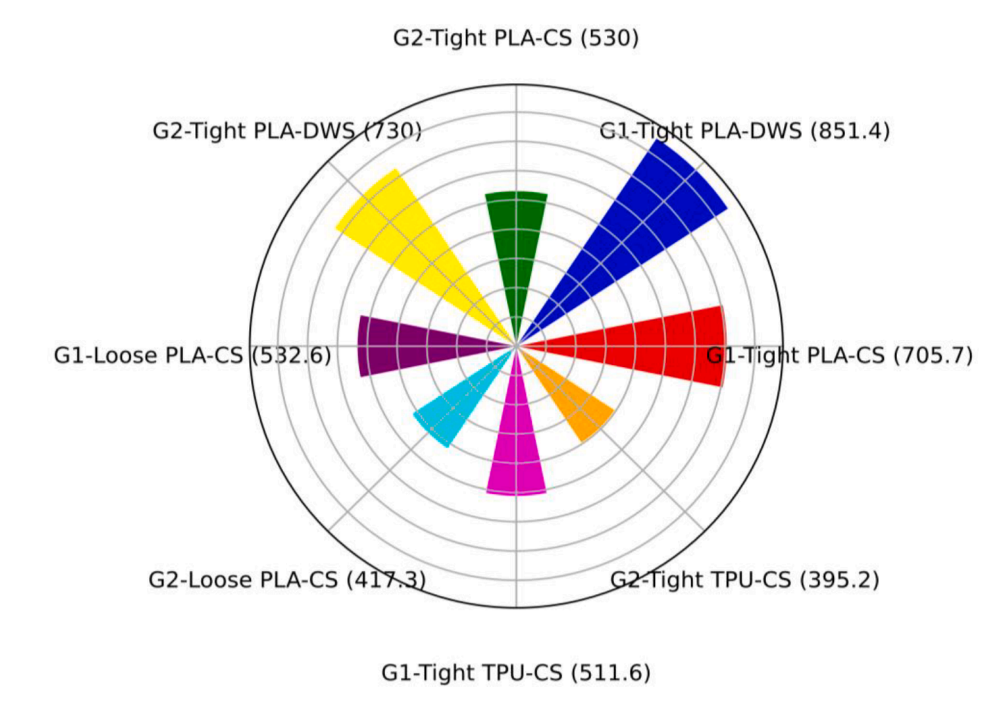


Fig. 16. Average compressive strength of all experiments with length to diameter ratio of 2.

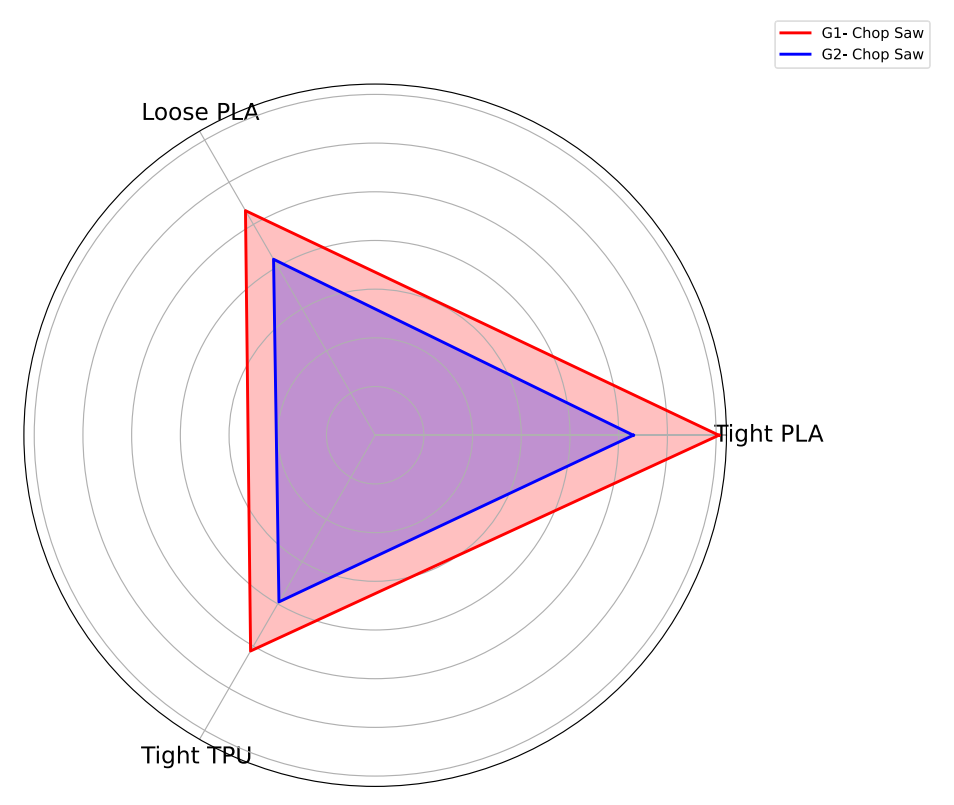


Fig. 17. Comparison of strength for different types of plugs.

Moreover, as PLA plugs are stiffer than TPU plugs, they deter samples from changing their position and causing eccentricities under loading. Quality of the cutting surfaces is crucial for applying load uniformly on the cross-section of the samples. Cutting the surface must be conducted in a way that creates two parallel surfaces on both ends of the samples. The compressive strength of GFRP bars is considerable, and neglecting it in designing procedures for compressive members, such as columns, is a

conservative practice. The obtained elastic modulus for G1 bars in compression showed that this value equals the tensile elastic modulus (58.7 MPa). Micro-CT scans revealed that the majority of the damage develops after reaching 75% of the ultimate capacity and propagates into inter-connected crack plates. The cracks at the endpoint of loading took up almost 13% of the overall sample volume and had a mean thickness of around 0.33 mm. The applicability of the proposed test

method to larger length-to-diameter ratios and bars with different surface enhancements such as sand-coated bars should be investigated.

# **Declaration of Competing Interest**

The authors declare that they have no known competing financial interests or personal relationships that could have appeared to influence the work reported in this paper.

# Data availability

Data will be made available on request.

## Acknowledgements

The authors would like to thank the National Science Foundation for financial support under grant number 1916342 and the Constructed Facilities Laboratory at North Carolina State University for providing the GFRP coupons. The micro-CT imaging was made possible by the National Science Foundation under the MRI award number 1920127.

#### References

- [1] M. Mirdarsoltany, A. Rahai, F. Hatami, R. Homayoonmehr, F. Abed, Investigating tensile behavior of sustainable basalt–carbon, basalt–steel, and basalt–steel-wire hybrid composite bars, Sustainability (switzerland) 13 (19) (2021).
- [2] Nanni A, De Luca A, Jawaheri Zadeh H. Reinforced Concrete with FRP Bars. Reinforced Concrete with FRP Bars. 2014.
- [3] A. Ruiz Emparanza, B. Mcmahon, A. Nanni, Basalt FRP reinforcement in concrete topping slabs in a commercial building - A sustainable and durable solution, Concr. Int. 1 (43) (2021) 28–33.
- [4] M. Ekenel, H. Roghani, F.D.C. y Basalo, A. Nanni, Evaluation of FRP Bars & meshes used as secondary reinforcement for nonstructural concrete members for building code compliance, Special Publ. 356 (2022) 109–119.
- [5] P.F. Castro, N.J. Carino, Tensile and nondestructive testing of FRP bars, J. Compos. Constr. 2 (1) (1998) 17–26.
- [6] J.P. Won, C.G. Park, J.C. Il, Tensile fracture and bond properties of ductile hybrid FRP reinforcing bars, Polym. Polym. Compos. 15 (1) (2007) 9–16.

- [7] C. Lu, M. Ni, T. Chu, L. He, Comparative investigation on tensile performance of FRP bars after exposure to water, seawater, and alkaline solutions, J. Mater. Civ. Eng. 32 (7) (2020), 04020170.
- [8] L. Alnajmi, F. Abed, Evaluation of FRP bars under compression and their performance in RC columns, Materials. 13 (20) (2020) 1–19.
- [9] F. Abed, Z. Mehaini, C. Oucif, A. Abdul-Latif, R. Baleh, Quasi-static and dynamic response of GFRP and BFRP bars under compression, Comp. Part C: Open Access. 1 (2020) 2.
- [10] Plevkov V, Baldin I, Kudyakov K, Nevskii A. Mechanical properties of composite rebar under static and short-term dynamic loading. AIP Conf Proc. 2017;1800 (January 2017).
- [11] Khan QS, Sheikh MN, Hadi MNS. Tension and compression testing of fibre reinforced polymer (FRP) bars [Internet]. 2015. Available from: https://ro.uow.ed u.au/eispapers/5008.
- [12] ASTM D695-15 Standard Test Method for Compressive Properties of Rigid Plastics Title. ASTM International. 2017.
- [13] D.H. Deitz, I.E. Harik, H. Gesund, Physical properties of glass fiber reinforced polymer rebars in compression, J. Compos. Constr. 7 (4) (2003) 363–366.
- [14] K. Khorramian, P. Sadeghian, Material characterization of GFRP bars in compression using a new test method, J. Test. Eval. (2019).
- [15] O. AlAjarmeh, A. Manalo, B. Benmokrane, P. Schubel, X. Zeng, A. Ahmad, et al., Compression behavior of GFRP bars under elevated In-Service temperatures, Constr. Build. Mater. 3 (2022) 314.
- [16] ACI Committee 440. Building Code Requirements for Structural Concrete Reinforced with Glass Fiber-Reinforced Polymer (GFRP) Bars: Code and Commentary. American Concrete Institute; 2022. 255 p.
- [17] S. Nolan, M. Rossini, F. Matta, A. Nanni, Overview of aashto LRFD bridge design guide specifications for GFRP reinforced concrete, Fib Symposium. (2018) 2302–2303
- [18] O.S. AlAjarmeh, A.C. Manalo, B. Benmokrane, P.V. Vijay, W. Ferdous, P. Mendis, Novel testing and characterization of GFRP bars in compression, Constr. Build. Mater. 225 (2019) 1112–1126.
- [19] ASTM D7957/D7957M-22 Standard Specification for Solid Round Glass Fiber Reinforced Polymer Bars for Concrete Reinforcement. ASTM International. 2022.
- [20] FDOT (2020) Section 932 Nonmetallic Accessory Materials for Concrete Pavement and Concrete Structures. FDOT Standard Specifications for Road and Bridge Construction Florida Department of Transportation, Tallahassee. 2022.
- [21] ASTM D792-20 Standard Test Methods for Density and Specific Gravity (Relative Density) of Plastics by Displacement. ASTM International. 2020.
- [22] ASTM D7205/D7205M-21 Standard Test Method for Tensile Properties of Fiber Reinforced Polymer Matrix Composite Bars. ASTM International, 2021.
- [23] D.S. Moore, G.P. McCabe, Introduction to the Practice of Statistics, WH Freeman and company, 2009.
- [24] M.H. DeGroot, M.J. Schervish, Probability and Statistics, 4th ed., Addison-Wesley, 2012.